Journal of Power Sources 271 (2014) 195–202

Contents lists available at ScienceDirect

Journal of Power Sources

journal homepage: www.elsevier.com/locate/jpowsour

Improved performance of CdS/CdSe quantum dots sensitized solar cell by incorporation of ZnO nanoparticles/reduced graphene oxide nanocomposite as photoelectrode

F.S. Ghoreishi [a], V. Ahmadi [b, *], M. Samadpour [c]

[a] Dept. of Nanotechnology Engineering, Tarbiat Modares University, Tehran, Iran
[b] Dept. of Electrical & Computer Engineering, Tarbiat Modares University, Tehran, Iran
[c] Dept. of Physics, K.N. Toosi University of Technology, Tehran, Iran

HIGHLIGHTS

- A new design is presented for QDSSCs photoanodes based on ZnO NPs/RGO nanocomposite.
- A simple method is used for ZnO NPs/RGO nanocomposite synthesis as photoanode layer.
- Interfacial charge recombination in photoanode is reduced due to the use of RGO.
- Electron diffusion length in photoanode is enhanced due to the use of RGO.
- 2.20% efficiency is obtained for ZnO NPs/RGO layer that is two times more than ZnO NPs layer one.

ARTICLE INFO

Article history:
Received 12 April 2014
Received in revised form
12 July 2014
Accepted 24 July 2014
Available online 1 August 2014

Keywords:
Graphene
Quantum dot sensitized solar cells
Nanocomposite
Cadmium sulfide
Cadmium selenide

ABSTRACT

Here we present novel quantum dot sensitized solar cells (QDSSC) based on ZnO nanoparticles (NPs)/reduced graphene oxide (RGO) nanocomposite photoanodes for better light harvesting and energy conversion. Photoelectrodes are prepared by doctor blading ZnO NPs/GO nanocomposite paste on a fluorine doped tin oxide substrate which are then sintered at 450 °C to obtain ZnO NPs/RGO nanocomposites. The partial reduction of GO after thermal reduction, is studied by Fourier transform infrared and Raman spectroscopies. Cadmium sulfide (CdS) and cadmium selenide (CdSe) quantum dots are deposited on the films through successive ionic layer adsorption and reaction and chemical bath deposition methods, respectively. The unique properties of ZnO NPs/RGO photoanodes, lead to a significant enhancement in the photovoltaic properties of solar cells in comparison with bare ZnO photoanodes. Current–voltage characteristics of cells are studied and the best results are obtained from ZnO NPs-RGO/CdS/CdSe with photoelectric conversion efficiency of 2.20% which is almost two times higher than cells which are made by pure ZnO NPs as photoanode (1.28%). Electrochemical impedance measurements show that the enhancement can be attributed to the increase of electron transfer rate in the ZnO NPs/RGO nanocomposite photoanode which arises from the ultrahigh electron mobility in graphene (RGO) sheets.

1. Introduction

Recently, inorganic and hybrid light absorbers such as quantum dots and organometal halide perovskites have been used in photovoltaic devices showing great possibility for a new large scale cost-competitive photovoltaic technology [1,2]. The attractiveness of the hybrid inorganic–organic perovskite semiconductors can be attributed to their direct band gap, large absorption coefficient [3], high carrier mobility [4], solution processability, and tunable optical and electronic properties [5] which make them very interesting as light harvesters in mesoscopic solar cells.

The power conversion efficiency of more than 15% is now achieved by different groups [6–9].

QDSSCs have attracted great attention as light absorbing materials for preparing high efficient and low cost photovoltaic cells [10]. Nanocrystal semiconductors (QDs) show several benefits such

* Corresponding author. Tel./fax: +98 21 82883368.
E-mail address: v_ahmadi@modares.ac.ir (V. Ahmadi).

http://dx.doi.org/10.1016/j.jpowsour.2014.07.165
0378-7753/

as; size-dependent band gaps [11], large intrinsic dipole moments [12,13] and higher extinction coefficients [14] as compared with metallorganic dyes. In addition, their ability to generate multiple excitons for a single photon [15,16], provides higher energy conversion efficiency beyond the Shockley–Queisser limit [17].

Among all the wide band gap semiconductors explored as alternatives to TiO_2 as an electron conductor, ZnO with a similar band gap (3.37 eV) and the richest family of nanostructures with wide range of synthesis methods [18], exhibits excellent electron mobility [19,20] .

Considering the unique sheet morphology, ultrahigh electron conductivity and mobility, graphene could be an efficient material for electron transport in energy industry such as inverted polymer solar cells [21,22], quantum dot solar cells [23] and hybrid light emitting diodes [24]. The efficiencies of QDSSCs based on bare ZnO layers are averagely low. The limiting parameter is usually attributed to electron accumulation in ZnO layer (photoanode) because of the nearly slow electron transfer [25] which results in charge recombination at the semiconductor–electrolyte interface. Hence, preventing charge recombination at the semiconductor–electrolyte interface is an important factor to enhance the performance of QDSSCs [26]. A few research groups have utilized graphene nanocomposites as the photoanode layer in QDSSCs [27,28]. Chen et al. have reported the application of graphene/ZnO nanorod composite architecture in CdSe QDSSCs [26]. In their work, ZnO nanorords have been used while in this study the nanoparticles of ZnO are used. The reason of our choice, is the larger specific surface area of nanoparticles compared to nanorods, which provides a larger area for quantum dots loading [19]. The higher efficiency of 1.28% for the cell with ZnO NPs photoanode compared to the 0.78% efficiency reported in Ref. [26] with the ZnO nanorods layer could be due to the use of ZnO nanoparticles instead of nanorods.

The highest efficiency obtained in this study in regard to the cell with ZnO NPs/RGO photoanode, is recorded as 2.20% while the highest efficiency in the Chen's article is equal to 1.7%. In fact, the device in our proposed architecture has led to a 30% enhancement of efficiency as compared with reference 17. Also the J_{sc} of the cell with ZnO NPs/RGO photoanode in our study (8.72 mA cm^{-2}) has a dramatic increase of 87% compared to the one in Ref. [26] (4.65 mA cm^{-2}).

In this paper, we propose and exhibit the use of a ZnO NPs/reduced graphene oxide (RGO) nanocomposite architecture to increase the electron transport in QDSSCs. Photovoltaic properties of cells with ZnO NPs/RGO photoanode are reported and discussed in comparison with cells with bare ZnO NPs photoanode. It was deduced that, the efficiency of cells with ZnO NPs/RGO structure is enhanced about twice the respective amount in the case of cells without RGO layers. To the extent of our knowledge, this is the first report on the application of the ZnO NPs/RGO nanocomposite as a photoanode in QDSSCs.

2. Experimental

2.1. Preparation of graphene oxide

Graphene oxide (GO) is prepared using the Hummers method by acid oxidation and exfoliation of graphite powder (Merck chemical) [29,30]. First, 2 g of graphite powders in 100 mL of concentrated H_2SO_4 (≥98%, Merck chemical) is stirred strongly. Eight grams (8 g) of $KMnO_4$ (≥99.5%, Merck chemical) is added slowly with stirring in an ice bath to keep the temperature of the mixture below 10 °C and the mixture is stirred in this condition for 2 h. Then, the mixture is additionally stirred at 35 °C for 1 h. After the reaction is completed, 100 mL of deionized (DI) water is poured into the mixture and mixed for another 1 h. The reaction is finished by adding 100 mL of DI water and 20 mL of 30% H_2O_2 (Merck chemical) solution. The final mixture is filtered, and rinsed with 5% HCl (Merck chemical) aqueous solution and DI water respectively. Finally, graphene oxide powder is collected after being dehydrated in the vacuum oven at 80 °C for 24 h [31].

2.2. Preparation of ZnO nanoparticles

The synthetic process of the ZnO nanoparticles (NPs) by direct precipitation method begins with dissolving $Zn(NO_3)_2$ (≥99.5%, Merck chemical) and $(NH_4)_2CO_3$ (≥99.0%, Merck chemical) in DI water to form 1.5 and 2.25 M solutions successively. The $Zn(NO_3)_2$ solution is gradually poured into the $(NH_4)_2CO_3$ solution along with intense stirring. Then the precipitates produced from the reaction between two solutions, are filtered and washed three times with DI water and ethanol (≥99.8%, Merck chemical), respectively. The precipitates are dried at 80 °C and finally sintered at 550 °C for 2 h [32].

2.3. Fabrication of ZnO NPs/reduced graphene oxide nanocomposite

Photoelectrodes are prepared by doctor blading ZnO NPs/GO nanocomposite paste on an FTO (fluorine doped tin oxide) substrate (glass/FTO 15 Ω, Dyesol Co.). First, GO and ZnO NPs nanopowders are mixed with ethanol and sonicated for 45 min. The ratio of ZnO NPs/GO is fixed on 222 [27]. Ethanolic solution of ethyl cellulose (ethoxyl basis, Aldrich) with 10 wt% is prepared and then mixed with ZnO NPs/GO solution and terpineol (≥ 95%, Fluka), to obtain a light gray slurry. After heating the slurry in a rotary evaporator, ethanol in the mixture is removed and finally ZnO NPs/GO paste is obtained. The final paste contains 18 wt% ZnO NPs/GO, 9 wt% ethyl cellulose and 73 wt% terpineol [33]. The paste is deposited on an FTO substrate by doctor blading method and then the deposited films are sintered at 450 °C for 90 min to form ZnO NPs/RGO photoelectrodes. The stated sintering temperature and time are not only enough for the removal of excess precursors from the paste but also adequate for the thermal reduction of GO into graphene (RGO) to take place [27]. The cell active area is 0.25 cm^2.

2.4. Sensitizing the photoelectrodes with quantum dots

CdS and CdSe QDs are grown directly on ZnO NPs/RGO nanocomposites and ZnO NPs films by successive ionic layer adsorption (SILAR) and chemical bath deposition (CBD) methods, respectively. Finally, ZnS is deposited by SILAR [34]. The SILAR method for CdS QDs synthesizing, involves immersing the ZnO NPs and ZnO NPs/RGO photoelectrodes in 0.05 M $Cd(NO_3)_2$ (≥99%, Merck Chemical) ethanol solution for 1 min, washing with ethanol and next, 1 min immersion in 0.05 M Na_2S (≥63%, Acros) methanol/DI water solution (50:50 v/v) and finally washing with methanol (≥98%, Merck Chemical). The whole process of immersions is considered as one SILAR cycle. SILAR cycles are repeated 10 times to form an efficient layer of CdS QDs on the films [35]. For deposition of CdSe QDs by the CBD method, a chemical solution is prepared by mixing 80 mM of $CdSO_4$ (≥98%, Merck Chemical) and 80 mM of Na_2SeSO_3 solutions with 120 mM of nitriloacetic acid (≥99%, Acros) [36]. The films are immersed in the formed solution at 10 °C for 24 h, and finally are washed with DI water and dried with N_2 gas. After CdSe sensitization, all the samples are covered with ZnS by immersion into 0.1 M $Zn(CH_3COO)_2$ (reagent grade, Merck Chemical) and 0.1 M Na_2S solutions for 1 min dip^{-1} successively, washing with DI water between dips. This procedure is repeated three times to make an efficient layer of ZnS. The Cu_2S as counter electrode is prepared by using four cycles of SILAR method with electrode dipping in

aqueous solutions of $Cu(NO_3)_2$ and Na_2S with 0.5 M concentration, respectively and is rinsed with DI water between each two immersions [34].

2.5. Device fabrication

The working electrodes (CdS/CdSe QD-sensitized ZnO NPs and ZnO NPs/RGO photoelectrodes) and the Cu_2S counter electrodes are sealed using a 30 μm thick spacer (solaronix). The polysulfide electrolyte is injected into the gap between the electrodes by a vacuum pump. Polysulfide electrolyte containing 1 M Na_2S, 1 MS (≥99.5%, Riedel-de Haën) and 0.1 M NaOH (≥99.5%, Merck chemical) is prepared in a 20 mL DI water solution [37]. The schematic image of the fabricated device is shown in Fig. 1.

2.6. Characterization

The crystallographic structures of the materials are characterized by a powder X-ray diffraction system (XRD, X'Pert MPD, Philips) equipped with Cu Kα radiation ($\lambda_o = 1.540$ Å). The morphology of the samples is investigated by scanning electron microscope (SEM, XL30 Philips). Fourier transform infrared (FTIR) spectra are measured with Frontier FTIR equipment from Perkin Elmer company spectrometer. Raman spectra are recorded with SENTERRA Raman spectrometer from BRUKER Company. The diffuse reflectance absorption spectra (DRS) are recorded by an UV–vis spectrophotometer (AvaSpec2048, Avantes) equipment. Electrochemical impedance spectroscopy (EIS) measurements are performed with an IVIUM stat (XRE model) potentiostat/galvanostat with the frequency range from 1 mHz to 100 kHz. Photocurrent–voltage (I–V) characteristics are recorded at a range of air mass 1.5 G illumination intensity using a solar simulator (SIM-10-2, SHARIF SOLAR).

3. Results and discussion

Fig. 2 depicts the XRD patterns of ZnO nanoparticles prepared by the calcination of $Zn_4CO_3(OH)_6 \cdot H_2O$ precursors at a temperature of 550 °C for 2 h. The ZnO nanoparticles have a wurtzite structure. All the diffraction peaks in Fig. 2 can be indexed to the hexagonal phase ZnO reported in the joint committee on powder diffraction standards (JCPDS) card (No. 36-1451) [32]. The average crystalline size of 50 nm is obtained from Debye–Scherrer formula for ZnO nanoparticles.

The SEM image of the synthesized ZnO nanoparticles is shown in Fig. 3. As can be seen the morphology of the ZnO nanoparticles

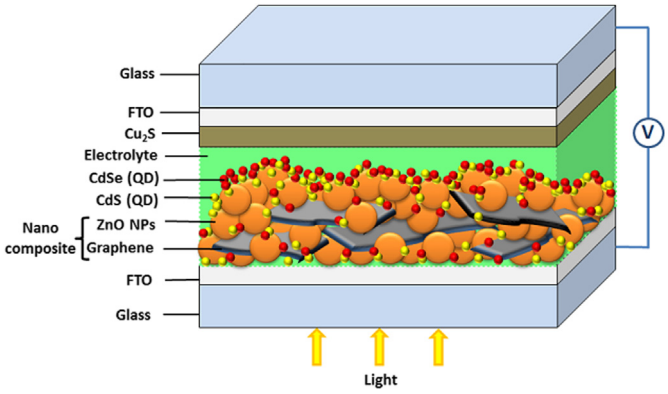

Fig. 1. The schematic diagram of QDSSC with ZnO NPs/RGO nanocomposite working electrode.

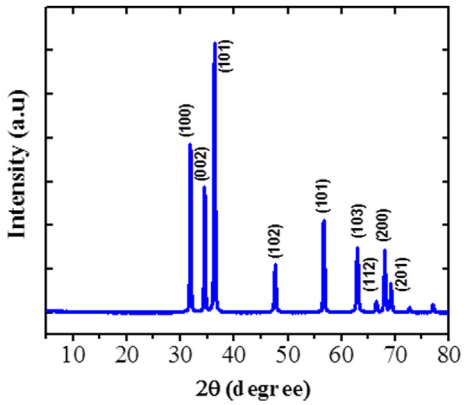

Fig. 2. XRD patterns of the ZnO nanoparticles. The crystal planes of ZnO are shown in the pattern.

possess pseudo-spherical shapes. The SEM image indicates that the average diameter of particles is in the range of 50 nm which is in good agreement with the value obtained from Scherrer formula.

The XRD patterns of natural graphite powder, GO and ZnO NPs/RGO layer coated on the FTO substrate are presented in Fig. 4. In the XRD spectrum of the natural graphite powder, a strong (002) peak at 26.54° appears, which indicates a typical pattern of crystal graphitic structure. GO has a diffraction peak at around $2\theta = 10.0°$, which is attributed to (001) reflection. In the ZnO NPs/RGO nanocomposite, this reflection peak of GO disappears due to the reduction of GO through the annealing and also break off of the ordered stack of GO by anchoring of ZnO nanoparticles [38].

The process of the thermal reduction of GO is then studied with FTIR and Raman spectroscopies. FTIR measurement is employed for investigating the bonding interactions in RGO before and after the thermal reduction, as shown in Fig. 5. In the FTIR spectrum of the GO, the strong and wide absorption peak placed on 3250 cm^{-1} is related to the stretching vibrations of O–H bonds. The peak at 1719 cm^{-1} is assigned to stretching vibrations of C=O in carboxylic acid and carbonyl groups located at the edges of GO sheets. The peak at 1602 cm^{-1} is also in reference to the vibrations of the absorbed water molecules and skeletal vibrations of unoxidized graphitic domains. The peaks at 1284 cm^{-1} and 1174 cm^{-1} are

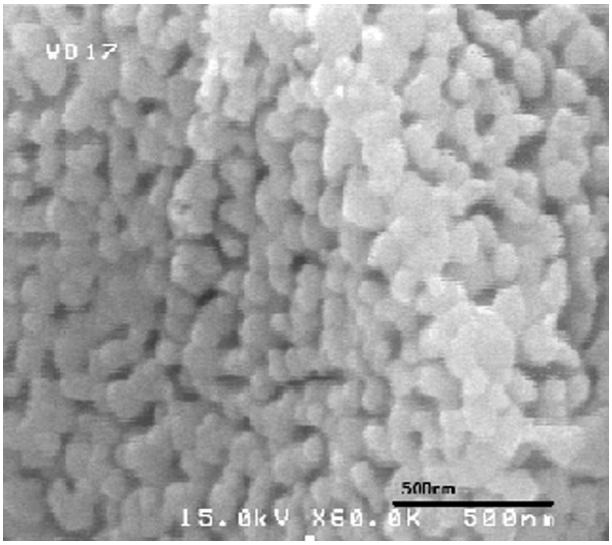

Fig. 3. SEM micrograph of ZnO nanoparticles.

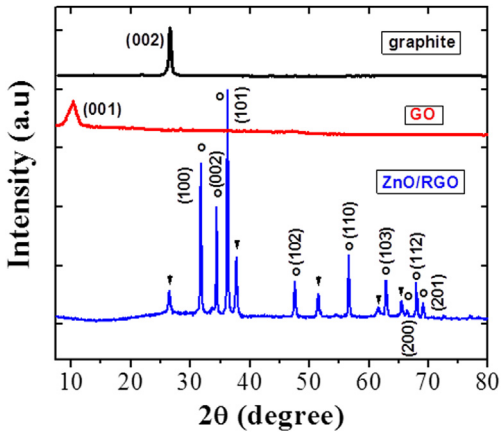

Fig. 4. XRD patterns of graphite powder, GO and the ZnO NPs/RGO nanocomposite coated on the FTO glass which revealing the peaks attributed to ZnO (○) and FTO (▼).

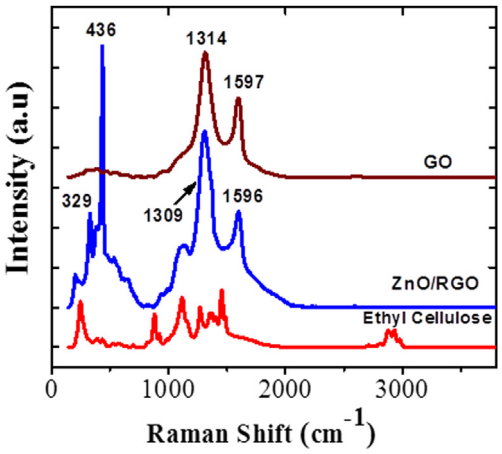

Fig. 6. Raman patterns of ethyl cellulose, GO and ZnO NPs/RGO.

usually related to the C–OH stretching vibrations and C–O–H vibrations, respectively. Also, the peak at 1069 cm^{-1} is attributed to C–O stretching vibrations (epoxy groups) [39].

FTIR spectra of RGO illustrates that O–H stretching vibrations situated at 3400 cm^{-1} are considerably reduced due to deoxygenation [40]. Comparing two spectra, it is noticeable that the peaks related to oxygen functional groups are almost removed in graphene oxide by annealing at 450 °C for 90 min.

These results show that the GO has been reduced considerably [41]. Besides, the absorption peak at around 575 cm^{-1} for the ZnO NPs/RGO, corresponds to the stretching vibration of Zn–O bond, which is blue-shifted from 410 cm^{-1} of Zn–O in the bulk ZnO [42].

Raman spectra of ethyl cellulose, GO and ZnO NPs/RGO powders are shown in Fig. 6. GO and ZnO NPs/RGO samples show two main peaks which are named the G and the D bands. The G band is caused by the in-plane stretching vibration of symmetric sp^2 C–C bonds, while the D band is the results of the disturbance of the hexagonal graphitic lattice [43]. The I_D/I_G intensity ratio increases slightly in the ZnO NPs/RGO nanocomposite compared with ZnO NPs/GO, (1.83 vs. 1.5), which indicates a decrease in the size of sp^2 domains upon reduction [44] and the interaction between ZnO nanoparticles and the reduced graphene oxide sheets [45]. This increment also shows the removal of oxygen functional groups in the GO and the reestablishment of the conjugated graphene network (sp^2 carbon) [45].

The peaks situated at the low frequencies (329 and 436 cm^{-1}) are the characteristic peaks of the ZnO with hexagonal wurtzite structure [46] which are pertained to the multiple-phonon scattering processes and E_2 (high) mode, respectively [44,45]. In the Raman spectrum of ZnO NPs/RGO sample there is a peak located at 1117 cm^{-1} which corresponds to ethyl cellulose powder (from the comparison of ethyl cellulose and ZnO NPs/RGO spectra). The appearance of this peak shows that ethyl cellulose is not removed completely from the paste through the annealing process.

The optical properties of FTO glasses coated with ZnO NPs and ZnO NPs/RGO layers are studied with UV–vis diffuse reflectance spectroscopy (DRS), as shown in Fig. 7. The film thickness for both ZnO NPs and ZnO NPs/RGO layers is 10 μm. Considering the DRS result of ZnO NPs sample, we can realize that the absorption edge starts at 400 nm [46]. The similar absorption edge of the ZnO NPs/RGO nanocomposite and the pure ZnO NPs shows that the band gap has not been changed [46]. However, the reflectance intensity decreases for ZnO NPs/RGO nanocomposite compared with ZnO NPs. With the same thickness (10 μm) and transmittance (equal to zero) for both layers, such a decrease can be due to higher absorption of RGO and the increase of surface electric charge in the nanocomposite which may lead to modification of the basic procedure of electron–hole pair formation during irradiation [47].

An energy level schematic diagram of the QDSSC comprised of FTO, graphene (RGO), ZnO nanoparticles, CdS and CdSe QDs and

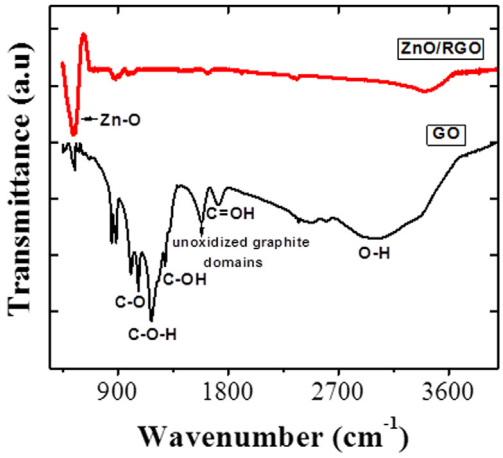

Fig. 5. FTIR spectra of GO and RGO.

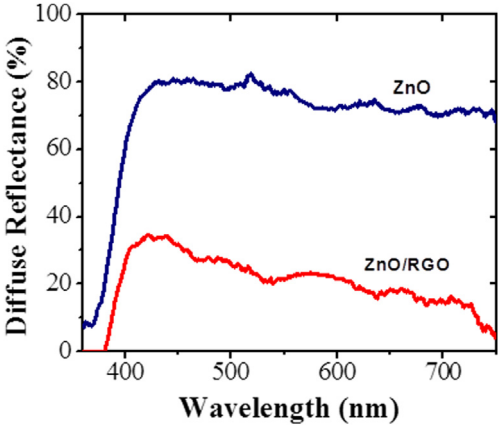

Fig. 7. UV–vis diffuse reflectance spectra (DRS) of ZnO NPs and ZnO NPs/RGO layers without quantum dot sensitizing.

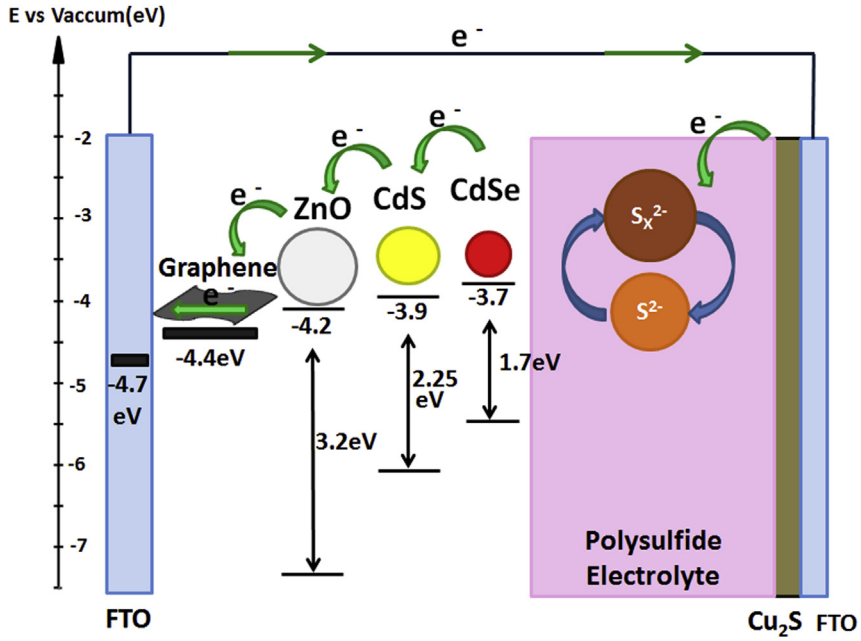

Fig. 8. The energy band illustration of ZnO-graphene/CdS/CdSe QDSSCs nanostructure.

polysulfide electrolyte, is presented in Fig. 8. The typical graphene has a work function equal to 4.4–4.5 eV [48]. The 0.2 eV offset between the ZnO conduction band and the graphene work function, leads to a lower barrier at their interface [26]. Regarding the energy levels shown in Fig. 8, it is obvious that the transfer of electron from CdSe QDs to the ZnO/graphene nanostructure is enhanced.

Fig. 9 shows the *I–V* curves of cells with ZnO NPs and ZnO NPs/RGO photoanodes, respectively under simulated 100 mW cm^{-2} illumination. The corresponding photovoltaic parameters of both cells are listed in Table 1. The cell with ZnO NPs photoanode exhibits J_{sc}, V_{oc} and conversion efficiency (η) of 8.43 mA cm^{-2}, 0.345 V and 1.28%, respectively, while the cell with ZnO NPs/RGO nanocomposite photoanode, exhibits J_{sc}, V_{oc} and η of 8.72 mA cm^2 0.57 V and 2.20%, respectively. The performance of solar cell with photoanode based on ZnO NPs is poor, because electrons accumulated in the ZnO due to the nearly slow electron transfer, lead to surface recombination [25]. The improved efficiency of cell with

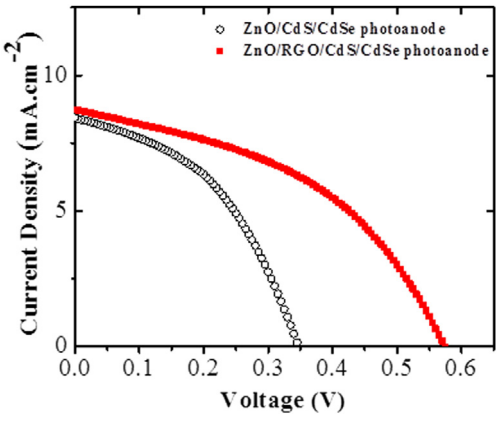

Fig. 9. *I–V* curves of ZnO NPs and ZnO NPs/RGO nanocomposite QDSSCs under 100 mW cm^{-2}, AM 1.5 simulated illuminations.

incorporation of graphene is due to unique characteristics of this nanomaterial. Ultrahigh electron mobility of graphene improves electron transfer properties at photoelectrode/electrolyte interface, resulting in lower recombination at ZnO interface and hence increasing the conversion efficiency of QDDSCs.

According to Table 1, while the fill factor and current density are almost the same in both cells with ZnO NPs/CdS/CdSe/ZnS and ZnO NPs-RGO/CdS/CdSe/ZnS photoanodes, the open circuit photovoltage of the cells with ZnO NPs/CdS/CdSe/ZnS photoanode is only 0.345 V which is noticeably lower than the photovoltage of the cells with ZnO NPs-RGO/CdS/CdSe/ZnS photoanode (0.57 V). This considerable reduction of photovoltage could occur due to various reasons such as Fermi level pinning in the photoanode that means the position of Fermi level in photoanode can't rise above a certain amount even with increasing the light intensity or applying more bias voltage. In this case the chemical capacitance of the cell is fixed in spite of the increase in bias voltage or light intensity [34,49]. Beside the Fermi level pinning, the low photovoltage in the cell could be originated from the intense charge recombination between the photoanode and the electrolyte. Therefore by scanning the bias voltage and monitoring the chemical capacitance of the cell, the mechanism of photovoltage enhancement in the cells with ZnO NPs-RGO/CdS/CdSe/ZnS photoanodes could be determined effectively.

For better understanding of RGO effects on the QDSSC performance, the electrochemical impedance spectroscopy (EIS) measurement is employed to gain more details about the carriers transport through the ZnO NPs and ZnO NPs/RGO QDSSCs. Nyquist plots for applied voltages between 0 and 0.5 V for ZnO NPs photoanode and 0 and 0.6 V for ZnO NPs/RGO photoanode are obtained. Nyquist curves are plotted for both cells in Fig. 10. The impedance spectra are fitted with the equivalent circuit shown in the Fig. 11 [54] by employing the Z-view software. R_s is the series resistance for the cell resulting from the contacts, C_μ is the chemical capacitance that is a function of the Fermi level and R_{rec} is the recombination resistance arisen by the charge transfer of electrons at the ZnO NPs or ZnO NPs-RGO/electrolyte interface [50].

Table 1
Photovoltaic parameters of the QDSSCs with ZnO NPs/CdS/CdSe and ZnO NPs/RGO/CdS/CdSe photoanodes, at 100 mW cm^{-2} light intensity.

Photoanode layer	J_{sc} (mA cm^{-2})	V_{oc} (V)	FF	Efficiency
ZnO/CdS/CdSe/ZnS	8.43	0.345	0.44	1.28%
ZnO-RGO/CdS/CdSe/ZnS	8.72	0.57	0.44	2.20%

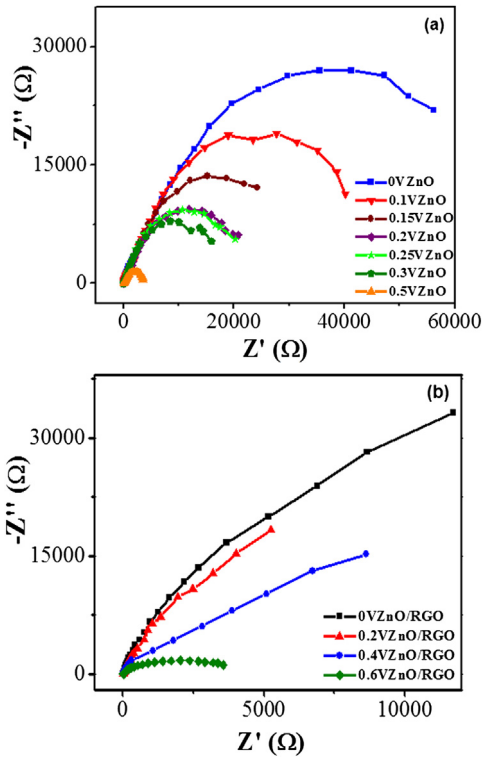

Fig. 10. Nyquist plots extracted from impedance measurement of (a) ZnO NPs and (b) ZnO NPs/RGO QDSSCs at different applied voltages (V_{app}) under dark conditions.

Here the series resistance (R_s), transport resistance (R_{tr}), recombination resistance (R_{rec}) and chemical capacitance (C_μ) are obtained directly by fitting the impedance spectra of the cells by the model shown in Fig. 11. Electron life time (τ_s) and electron diffusion length (D_L) in the photoanodes are obtained from the measured R_s, R_{tr}, R_{rec} and C_μ through using the equations proposed in Refs. [51,52].The curves shown in Fig. 10(a) and (b) correspond to the middle-frequency region for both ZnO NPs and ZnO NPs/RGO cells, respectively. The middle-frequency region is associated with the charge-transfer process (or charge recombination process) at the ZnO/electrolyte interface. The diameter of these quasi semi-circle curves is represented by R_{rec} [50]. An increase in diameter of quasi semi-circle curves in this region for ZnO NPs/RGO cell compared to that of bare ZnO NPs cell accounts for a higher interfacial electron recombination resistance at the interface between ZnO NPs/RGO photoanode electrode and polysulfide electrolyte. This results in decreased electron transfer rate at the photoanode/electrolyte interface.

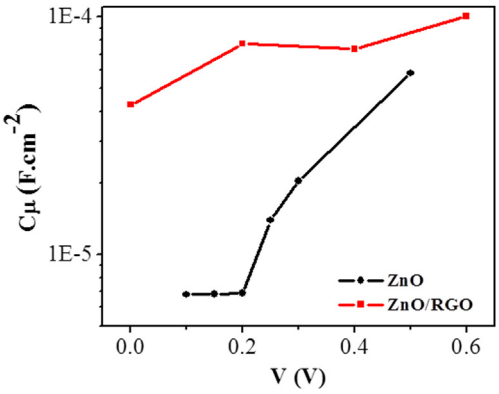

Fig. 12. Chemical capacitance curve obtained from impedance measurements for QDSSCs prepared with ZnO NPs and ZnO NPs/RGO photoelectrodes sensitized with CdS/CdSe QDs at different applied voltages.

Fig. 12 plots C_μ value for complete ZnO NPs and ZnO NPs/RGO QDSSCs as a function of the applied voltage in the CdS/CdSe sensitized electrodes. As can be seen, the C_μ value for ZnO NPs/RGO photoanode is dramatically increased compared to ZnO NPs photoanode. The chemical capacitance C_μ is defined as.

$$C_\mu = C_o \exp\frac{[E_{Fn} - E_{CB}]}{K_B T} \quad (1)$$

where C_0 is the chemical capacitance at zero bias potential, E_{Fn} and E_{CB} are the Fermi level and the conduction band edge energy, respectively and K_BT is regarded as the thermal energy.

According to Eq. (1), C_μ is a function of Fermi level. Thus, the increased chemical capacitance of the cell with ZnO NPs/RGO photoanode compared to the pure ZnO NPs, assuming constant conduction band edge, shows the rise of Fermi level which leads to an increase in the open circuit voltage and conversion efficiency of the cell with ZnO NPs/RGO photoanode [53]. According to Fig. 12, by increasing the voltage from 0.1 V to 0.5 V in the cells with ZnO NPs/CdS/CdSe/ZnS photoanode, chemical capacitance has increases accordingly. This result indicates that the Fermi level is not pinned in the ZnO NPs/CdS/CdSe/ZnS photoanode and another reason must be ascribed to the low photovoltage in these cells.

The recombination resistance (R_{rec}) at the photoanode and electrolyte interface and electron life time in photoanodes for ZnO

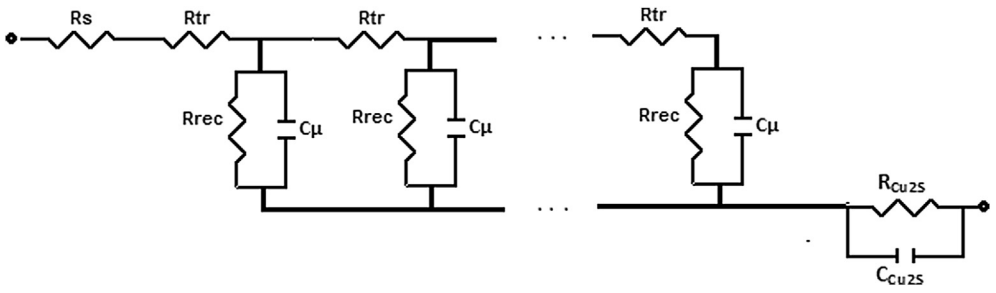

Fig. 11. The equivalent circuit used for fitting the impedance spectra.

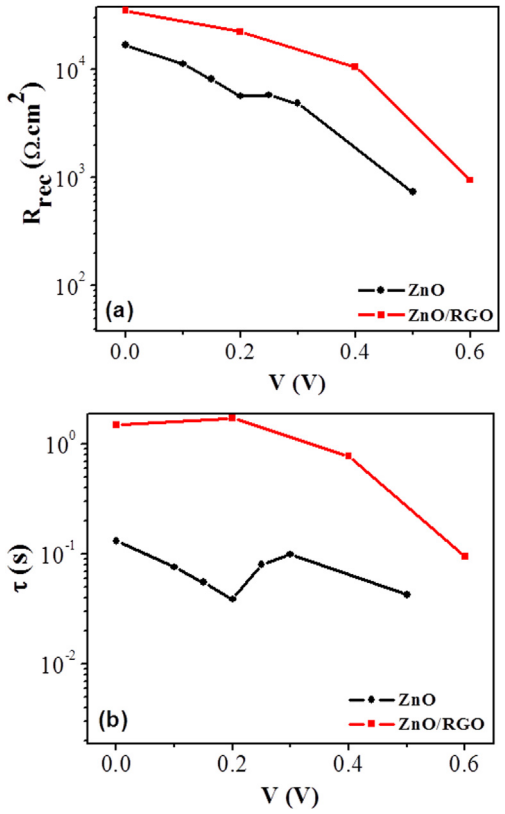

Fig. 13. (a) Recombination resistance, R_{rec} and (b) Electron life time, τ, obtained from EIS measurements for QDSSCs prepared with bare ZnO NPs and ZnO NPs/RGO photoanodes sensitized with CdS/CdSe QDs.

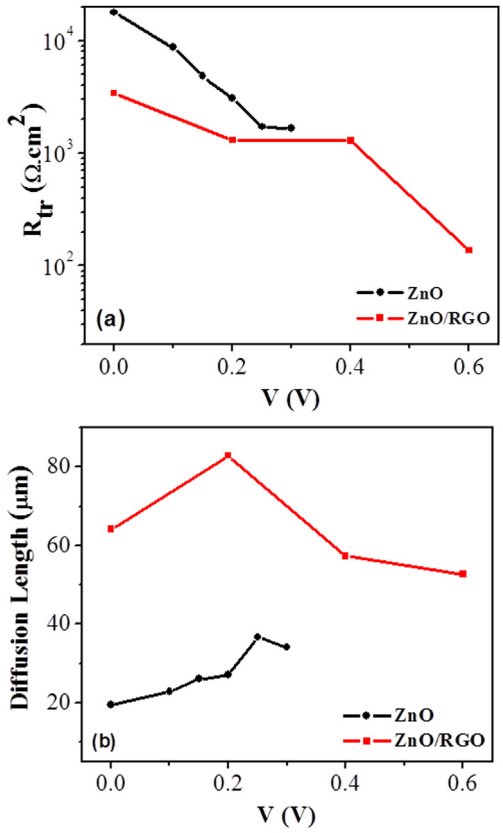

Fig. 14. (a) Electron transport resistance (R_{tr}) and (b) electron diffusion length, D_L, obtained from EIS measurements for QDSSCs prepared with bare ZnO NPs and ZnO NPs/RGO photoanodes sensitized with CdS/CdSe QDs.

NPs and ZnO NPs/RGO layers are plotted in Fig. 13(a) and (b), respectively. Electron life time (τ_s) is the time that an electron can be in the photoanode before it recombines with the electrolyte. Electron life time is inversely proportional to the electron recombination rate at the interface of photoanode and electrolyte. It can be obtained by measuring the recombination resistance (R_{rec}) and chemical capacitance (C_μ) from the EIS experiment and using the relation $\tau_s = R_{rec} \times C_\mu$ [50].

According to Fig. 13(a), R_{rec} of ZnO NPs/RGO nanocomposite layer has dramatically increased in comparison to ZnO NPs layer. This increment in R_{rec} results in lower electron recombination rate at the interface of photoanode and electrolyte and consequently increases the electron life time in photoanode (Fig. 13(b)) [54]. This in turn, leads to higher open circuit photovoltage in nanocomposite cells (Table 1) as compared to the cell with bare ZnO NPs.

Electron transport resistance (R_{tr}) and electron diffusion length (D_L) in photoanodes are shown in Fig. 14(a) and (b), respectively. As can be seen in Fig. 14(a), RGO with its high electron transport ability, results in the reduction of electron transport resistance (R_{tr}) in photoanode and enhancement of electron diffusion length (Fig. 14(b)) [50]. This leads to the increase of short circuit current and finally higher conversion efficiency in cells with ZnO NPs/RGO photoanode (Table 1). The sharp increase in electron life time for cells with ZnO NPs photoanode at 0.2 V is related to the recombination through surface states as discussed in Ref. [49].

4. Conclusion

We fabricated novel QDSSCs based on ZnO NPs/RGO nanocomposite photoanodes. The ZnO NPs/RGO nanocomposite film was used as the semiconductor layer and CdS/CdSe QDs were used as the sensitizing layer to prepare the photoanode of a QDSSC. The surface morphology, structure and photovoltaic properties of pure ZnO NPs and ZnO NPs/RGO nanocomposites were analyzed. The cell with ZnO NPs-RGO/CdS/CdSe photoanode showed a high efficiency of 2.20%, which was almost two times higher than that of the cell with bare ZnO NPs (1.28%). The improved efficiency of ZnO NPs-RGO photoanode was mainly caused by the incorporation of graphene (RGO) with high electron mobility and conductivity in the structure. This led to the enhancement of electron transport, suppressed charge recombination and longer electron life time in the cell, which was confirmed with the EIS method. It was shown that graphene (RGO), plays an advantageous role in assisting charge transportation and reduction of interfacial charge recombination which leads to enhanced power conversion efficiency. These results show that incorporation of graphene (RGO) sheets is an efficient way for enhancing the photovoltaic performance of QDSSCs.

Acknowledgment

The authors acknowledge the Iran Nanotechnology Initiative Council (INIC) for the partial support of this project.

References

[1] W. Zhang, M. Saliba, S.D. Stranks, Y. Sun, X. Shi, U. Wiesner, H.J. Snaith, Nano Lett. 13 (2013) 4505–4510.
[2] J. Bisquert, J. Phys. Chem. Lett. 4 (2013) 2597–2598.
[3] A. Kojima, M. Ikegami, K. Teshima, T. Miyasaka, Chem. Lett. 41 (2012) 397–399.
[4] C. Kagan, D. Mitzi, C. Dimitrakopoulos, Science 286 (1999) 945–947.

[5] L. Etgar, P. Gao, Z. Xue, Q. Peng, A.K. Chandiran, B. Liu, M.K. Nazeeruddin, M. Grätzel, J. Am. Chem. Soc. 134 (2012) 17396–17399.
[6] S. Kazim, M.K. Nazeeruddin, M. Grätzel, S. Ahmad, Angew. Chem. Int. Ed. 53 (2014) 2812–2824.
[7] P.V. Kamat, J. Am. Chem. Soc. 136 (2014) 3713–3714.
[8] J. Burschka, N. Pellet, S.-J. Moon, R. Humphry-Baker, P. Gao, M.K. Nazeeruddin, M. Grätzel, Nature 499 (2013) 316–319.
[9] P.V. Kamat, J. Phys. Chem. Lett. 4 (2013) 3733–3734.
[10] D.R. Baker, P.V. Kamat, Adv. Funct. Mater. 19 (2009) 805–811.
[11] W.W. Yu, L. Qu, W. Guo, X. Peng, Chem. Mater. 15 (2003) 2854–2860.
[12] R. Vogel, P. Hoyer, H. Weller, J. Phys. Chem. 98 (1994) 3183–3188.
[13] C. Justin Raj, S. Karthick, S. Park, K. Hemalatha, S.K. Kim, K. Prabakar, H.J. Kim, J. Power Sources 248 (2014) 439–446.
[14] P. Wang, S.M. Zakeeruddin, J.E. Moser, R. Humphry-Baker, P. Comte, V. Aranyos, A. Hagfeldt, M.K. Nazeeruddin, M. Grätzel, Adv. Mater. 16 (2004) 1806–1811.
[15] R.J. Ellingson, M.C. Beard, J.C. Johnson, P. Yu, O.I. Micic, A.J. Nozik, A. Shabaev, A.L. Efros, Nano Lett. 5 (2005) 865–871.
[16] R.D. Schaller, V.I. Klimov, Phys. Rev. Lett. 92 (2004) 186601.
[17] I. Concina, N. Memarian, G. Selopal, M. Natile, G. Sberveglieri, A. Vomiero, J. Power Sources 240 (2013) 736–744.
[18] K. Yu, J. Chen, Nanoscale Res. Lett. 4 (2009) 1–10.
[19] Q. Zhang, C.S. Dandeneau, X. Zhou, G. Cao, Adv. Mater. 21 (2009) 4087–4108.
[20] R. Jose, V. Thavasi, S. Ramakrishna, J. Am. Ceram. Soc. 92 (2009) 289–301.
[21] A. Chuchmała, M. Palewicz, A. Sikora, A. Iwan, Synth. Met. 169 (2013) 33–40.
[22] Y.J. Jeon, J.M. Yun, D.Y. Kim, S.I. Na, S.S. Kim, Sol. Energy Mater. Sol. Cells 105 (2012) 96–102.
[23] J.G. Radich, R. Dwyer, P.V. Kamat, J. Phys. Chem. Lett. 2 (2011) 2453–2460.
[24] J.M. Lee, J.W. Choung, J. Yi, D.H. Lee, M. Samal, D.K. Yi, C.H. Lee, G.C. Yi, U. Paik, J.A. Rogers, Nano Lett. 10 (2010) 2783–2788.
[25] I. Robel, V. Subramanian, M. Kuno, P.V. Kamat, J. Am. Chem. Soc. 128 (2006) 2385–2393.
[26] J. Chen, C. Li, G. Eda, Y. Zhang, W. Lei, M. Chhowalla, W.I. Milne, W.-Q. Deng, Chem. Commun. 47 (2011) 6084–6086.
[27] X. Fang, M. Li, K. Guo, Y. Zhu, Z. Hu, X. Liu, B. Chen, X. Zhao, Electrochim. Acta 65 (2012) 174–178.
[28] G. Zhu, T. Xu, T. Lv, L. Pan, Q. Zhao, Z. Sun, J. Electroanal. Chem. 650 (2011) 248–251.
[29] W.S. Hummers, R.E. Offeman, J. Am. Chem. Soc. 80 (1958), 1339–1339.
[30] G. Eda, G. Fanchini, M. Chhowalla, Nat. Nanotechnol. 3 (2008) 270–274.
[31] Y. Yang, L. Ren, C. Zhang, S. Huang, T. Liu, ACS Appl. Mater. Interfaces 3 (2011) 2779–2785.
[32] C. Chen, P. Liu, C. Lu, Chem. Eng. J. 144 (2008) 509–513.
[33] S. Ito, T.N. Murakami, P. Comte, P. Liska, C. Grätzel, M.K. Nazeeruddin, M. Grätzel, Thin Solid Films 516 (2008) 4613–4619.
[34] P. Sudhagar, T. Song, D.H. Lee, I. Mora-Seró, J. Bisquert, M. Laudenslager, W.M. Sigmund, W.I. Park, U. Paik, Y.S. Kang, J. Phys. Chem. Lett. 2 (2011) 1984–1990.
[35] H. Chen, L. Zhu, H. Liu, W. Li, J. Power Sources 245 (2013) 406–410.
[36] P.V. Kamat, K. Tvrdy, D.R. Baker, J.G. Radich, Chem. Rev. 110 (2010) 6664–6688.
[37] K. Meng, P.K. Surolia, O. Byrne, K.R. Thampi, J. Power Sources 248 (2014) 218–223.
[38] J. Liu, H. Bai, Y. Wang, Z. Liu, X. Zhang, D.D. Sun, Adv. Funct. Mater. 20 (2010) 4175–4181.
[39] S. Verma, H.P. Mungse, N. Kumar, S. Choudhary, S.L. Jain, B. Sain, O.P. Khatri, Chem. Commun. 47 (2011) 12673–12675.
[40] E.-Y. Choi, T.H. Han, J. Hong, J.E. Kim, S.H. Lee, H.W. Kim, S.O. Kim, J. Mater. Chem. 20 (2010) 1907–1912.
[41] D. Boukhvalov, M. Katsnelson, Phys. Rev. B: Condens. Matter 78 (2008) 085413.
[42] Q.P. Luo, X.Y. Yu, B.X. Lei, H.Y. Chen, D.B. Kuang, C.Y. Su, J. Phys. Chem. C 116 (2012) 8111–8117.
[43] N.J. Bell, Y.H. Ng, A. Du, H. Coster, S.C. Smith, R. Amal, J. Phys. Chem. C 115 (2011) 6004–6009.
[44] D.R. Dreyer, S. Park, C.W. Bielawski, R.S. Ruoff, Chem. Soc. Rev. 39 (2010) 228–240.
[45] S. Stankovich, D.A. Dikin, R.D. Piner, K.A. Kohlhaas, A. Kleinhammes, Y. Jia, Y. Wu, S.T. Nguyen, R.S. Ruoff, Carbon 45 (2007) 1558–1565.
[46] T. Xu, L. Zhang, H. Cheng, Y. Zhu, Appl. Catal. B: Environ. 101 (2011) 382–387.
[47] X. Liu, L. Pan, Q. Zhao, T. Lv, G. Zhu, T. Chen, T. Lu, Z. Sun, C. Sun, Chem. Eng. J. 183 (2012) 238–243.
[48] Y.-B. Tang, C.-S. Lee, J. Xu, Z.-T. Liu, Z.-H. Chen, Z. He, Y.-L. Cao, G. Yuan, H. Song, L. Chen, Acs Nano 4 (2010) 3482–3488.
[49] I. Mora-Seró, S. Giménez, F. Fabregat-Santiago, R. Gómez, Q. Shen, T. Toyoda, J. Bisquert, Acc. Chem. Res. 42 (2009) 1848–1857.
[50] F. Fabregat-Santiago, J. Bisquert, G. Garcia-Belmonte, G. Boschloo, A. Hagfeldt, Sol. Energy Mater. Sol. Cells 87 (2005) 117–131.
[51] J. Nissfolk, Department of Chemistry, KTH, 2009, pp. 1–60.
[52] M. Adachi, M. Sakamoto, J. Jiu, Y. Ogata, S. Isoda, J. Phys. Chem. B 110 (2006) 13872–13880.
[53] J. Bisquert, Phys. Chem. Chem. Phys. 5 (2003) 5360–5364.
[54] V. González-Pedro, X. Xu, I. Mora-Sero, J. Bisquert, ACS Nano 4 (2010) 5783–5790.